TOWARDS ADVERSARIALLY ROBUST DEEPFAKE DETECTION: AN ENSEMBLE APPROACH

Anonymous authors
Paper under double-blind review

ABSTRACT

Detecting deepfakes remains an open problem. Current detection methods fail against an adversary who adds imperceptible adversarial perturbations to the deepfake to evade detection. We propose **D**isjoint **D**eepfake **D**etection (D3), a deepfake detector designed to improve adversarial robustness beyond de facto solutions such as adversarial training. D3 uses an ensemble of models over disjoint subsets of the frequency spectrum to significantly improve robustness. Our key insight is to leverage a redundancy in the frequency domain and apply a saliency partitioning technique to disjointly distribute frequency components across multiple models. We formally prove that these disjoint ensembles lead to a reduction in the dimensionality of the input subspace where adversarial deepfakes lie. We then empirically validate the D3 method against white-box attacks and black-box attacks and find that D3 significantly outperforms existing state-of-the-art defenses applied to deepfake detection.

1 INTRODUCTION

Significant advances in deep learning are responsible for the advent of "deepfakes", which broadly refer to digital media that has been synthetically generated or modified by deep neural networks (DNNs). Modern DNNs such as generative adversarial networks (GANs) (Goodfellow et al., 2014) and auto-encoders (Baldi, 2012) are now capable of crafting hyper-realistic images and videos that are indistinguishable from real content. This has led to a rising concern of bad actors that can misuse deepfakes to craft fake social media profiles (Martineau, 2019), generate pornography (Cole, 2017), spread political propaganda, and even manipulate elections.

In response, recent work has attempted to solve the deepfake detection problem, in which a defender attempts to classify given media as deepfake or real. The state-of-the-art detection schemes often leverage DNNs on the frequency space of the input image. For example, Frank et al. (2020) proposed the use of DNNs to detect deepfakes with the Discrete Cosine Transform (DCT) as a preprocessing transform. Unfortunately, Carlini & Farid (2020) and Neekhara et al. (2021) showed that defenses fail because the adversary can simply use adversarial perturbation techniques to evade detection (Szegedy et al., 2014; Goodfellow et al., 2015; Biggio et al., 2013; Carlini & Wagner, 2017). Defending against adversarial examples, in general, has been shown to be a difficult task (Athalye et al., 2018), and is unexplored in the deepfake detection setting.

Our key intuition to mitigate this problem is to utilize *redundant information in the frequency feature space* of deepfakes to generate *disjoint ensembles* for deepfake detection. Specifically, we show in Section 3.1 that we can achieve good detection performance with only a subset of the features, particularly in the frequency domain. This enables us to build an ensemble of performant classifiers, each using a disjoint set of frequencies. In contrast to traditional ensembles (where each model shares the same set of frequencies), a key advantage of this design is that non-robust frequencies are partitioned across all the models in the ensemble. Thus, an adversary is no longer able to perturb a single non-robust frequency to evade all models — rather, they must find perturbations to evade multiple sets of disjoint frequencies, which raises the attack cost.

We leverage the above intuition to propose D3 (Disjoint Deepfake Detection). Our contributions are as follows:

1. We propose D3, the first deepfake detection framework designed to be adversarially robust. D3 builds a robust ensemble of models that use disjoint partitions of the input features. This is achieved by leveraging redundancy in the feature space. D3 achieves robustness while still exhibiting natural deepfake detection AUC-ROC scores as high as 99% (see Section 4.2 for details).
2. Extending the theoretical results by Tramèr et al. (2017b) on dimensionality of adversarial subspaces, we prove new bounds on the maximum number of adversarial directions that can be found under an ensemble with disjoint inputs. Our bounds are tight for both the ℓ_2 and ℓ_∞ perturbation norms (Lemmas 3.1 and 3.2 in Section 3.4) and indicate that D3 reduces the dimension of the adversarial subspace.
3. We evaluate D3 against white-box and black-box attacks on a variety of GAN-generated deepfake images. D3 significantly outperforms state-of-the-art defenses such as ADP (Pang et al., 2019), GAL (Kariyappa & Qureshi, 2019) and DVERGE (Yang et al., 2020), suggesting a reduction in dimensions of the adversarial subspace. For example, as indicated by our evaluation in Section 4.3, D3 maintains 100% adversarial accuracy against AutoAttack (Croce & Hein, 2020b) where baselines drop below 20%. Increasing the number of attack steps to 1000 reduces D3's robustness to 61% in comparison to 0% for all baselines. These results suggest that D3 is harder to attack than existing defenses.

2 Background and Related Work

Notation. We consider a distribution $\mathcal{D}$ over $\mathcal{X} \times \mathcal{Y}$, where $\mathcal{X} \in \mathbb{R}^d$ is the input space and $\mathcal{Y} \in \mathbb{Z}^c$ is the finite class-label space. We denote vectors in boldface (e.g., $\mathbf{x}$). We denote a trained classifier as a function $\mathcal{F} : \mathcal{X} \to \mathcal{Y}$ (the classifier is usually parameterized by its weights w, omitted for brevity). We denote the loss function as $\mathcal{L}(\mathbf{x}, y)$. An ensemble classifier is a function $M_{(\mathcal{F}_1,\mathcal{F}_2,...,\mathcal{F}_n)} : \mathcal{X} \to \mathcal{Y}$ that combines the logit outputs $l_1, l_2, ..., l_n$ of multiple classifiers $\mathcal{F}_1, \mathcal{F}_2, ..., \mathcal{F}_n$ with a voting aggregation function $\mathcal{A} : \mathbb{R}^{n\times c} \to \mathcal{Y}$.

For a classifier $\mathcal{F}$ and input-label pair $(\mathbf{x}, y)$, an adversarial example is a perturbed input $\mathbf{x}'$ such that (1) $\mathbf{x}'$ is misclassified, i.e., $\mathcal{F}(\mathbf{x}') \neq y$ and (2) $||\mathbf{x} - \mathbf{x}'||$ is within a small ϵ ball, where $||.||$ is a given norm. The value of ϵ is chosen to be small so that the perturbation is imperceptible to humans.

Deepfake Detection. The research community has taken several steps towards detecting GAN-generated deepfake images. Examples of proposed detection schemes include DNN classifiers (Wang et al., 2020; Yu et al., 2019), color-space anomaly detection (McCloskey & Albright, 2018), and co-occurrence matrix analysis (Nataraj et al., 2019). However, more recent work has significantly advanced the state-of-the-art for deepfake detection by leveraging *frequency-space analysis*. For example, Frank et al. (2020) proposed the idea of detecting deepfakes with the Discrete Cosine Transform (DCT) as a pre-processing transform before a binary DNN-based deepfake classifier. Similar work has also achieved remarkable performance — Zhang et al. (2019) use GAN simulators to extract similar frequency artifacts, and Durall et al. (2019) successfully train DNNs in the frequency domain to detect deepfakes. Unfortunately, Carlini & Farid (2020) showed that frequency-based detectors are vulnerable to adversarial examples – an adversary can add imperceptible adversarial perturbations to a deepfake that evade such detectors, rendering them ineffective.

Adversarial Training. A widely accepted solution to countering adversarial examples is to train the model on adversarial examples, generated during training (Madry et al., 2018). However, Carlini & Farid (2020) suggest that adversarial training alone is unlikely to achieve significant improvement in robustness in the difficult deepfake detection setting. Our experiments in Section 4.3 confirm that Frank et al. (2020)'s frequency-space deepfake detector, even when adversarially trained, cannot withstand deepfake examples crafted using a variety of attacks (see Tables 1 and 2). While we also adversarially train each model in our ensembles, we find that our ensembles significantly improve robustness over a standalone adversarially trained model (see Section 4.3).

Ensemble Defenses. A defender can also use an ensemble of models (Pang et al., 2019; Kariyappa & Qureshi, 2019; Yang et al., 2021). In principle, the adversary is then forced to attack multiple models, instead of just one. However, He et al. (2017) have shown that arbitrarily ensembling models does not necessarily lead to more robust defenses. One reason for this (as per Ilyas et al. (2019)) is that each model tends to learn the same non-robust features, i.e., an adversary is able

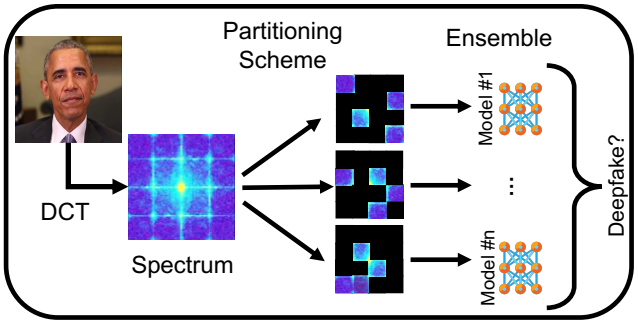

Figure 1: The processing pipeline of D3. It partitions the DCT spectrum of an image into disjoint partitions using either randomized or saliency-based approaches. Each frequency partition is fed to a separate model that is adversarially trained. A voting mechanism over the ensemble decides the output.

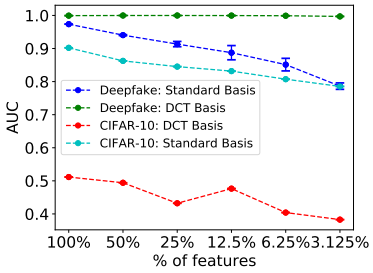

Figure 2: AUC-ROC scores of a single CNN classifier trained on a fixed subset (randomly selected) of the input features. Redundancy in frequency spectra permits near-perfect deepfake detection even when using $\sim 3\%$ of the components (see green line).

to perturb the same feature to evade all models. Recent efforts at adversarially robust ensembles have attempted to mitigate this phenomenon by introducing additional regularizers to the training process (Pang et al., 2019; Kariyappa & Qureshi, 2019; Yang et al., 2021). In contrast, we avoid this problem in deepfake detection "for free" via our frequency-partitioning approach to ensembles (see Section 3 for a more detailed explanation).

3 Our Approach

In the following, we present D3 (Figure 1), an ensemble deepfake detection framework that leverages disjoint frequency models to achieve robust deepfake detection. Section 3.1 presents our observation of redundant information in the frequency space of deepfakes. Section 3.2 details how redundancy allows frequencies to be partitioned between multiple models for robust ensembling. Finally, Section 3.3 explains our exact frequency partitioning schemes, and Section 3.4 provides theoretical insights into why D3 improves adversarial robustness.

3.1 Redundant Information in Deepfake Image Spectra

As discussed in Section 2, ensembles are a promising approach to adversarial robustness, so long as perturbing the same set of features does not simultaneously evade the individual models. We propose designing an ensemble that avoids this shortcoming by *disjointly partitioning the input feature space* amongst individual models.

Unfortunately, for traditional image classifications tasks like CIFAR10 (Krizhevsky et al., 2009) and ImageNet (Deng et al., 2009), a disjoint partitioning is likely to hurt natural classification performance, as partitioning results in information loss for each model. We visualize this phenomenon for CIFAR10 via the red and teal lines in Figure 2, which plots the worsening performance of a simple convolutional classifier [1] using increasingly small subsets of the input features (pixel or frequency).

Our first key insight is that, unlike traditional image classification tasks, disjoint partitioning is feasible for deepfake detection. Specifically, we observe a "redundancy" in frequency-space artifacts — signals relevant for deepfake detection [2] are distributed throughout the frequency spectrum. This observation is best exemplified by the green line in Figure 2, which plots the deepfake detection performance using increasingly small subsets of the spectrum using the same classifier. Using as few as $\sim 3\%$ of the frequency components yields near-perfect deepfake detection performance. We

[1] We use the same architecture for our primary defense implementation; details are provided in Section 4.1

[2] Frank et al. (2020) show that these artifacts manifest in the form of a grid-like spectral pattern, and attribute their presence to the upsampling process in generative models. Existing work proposes detectors that leverage the *entire frequency spectrum* for deepfake detection.

emphasize that this does not hold for subsets of pixels (blue line), as signals for detection are not well-distributed in the RGB space. Thus, the frequency-space contains plenty of redundancy, which can potentially be leveraged to design a robust ensemble.

3.2 Leveraging Redundancy to Build a Robust Ensemble

As discussed in Section 3.1, we aim to disjointly partition the frequency components amongst multiple detector models. Figure 1 visualizes this partitioning scheme as a part of our ensembling pipeline. Specifically, for each individual model we mask (i.e., zero out) the frequencies not used. For example, consider an ensemble of two such "disjoint" models F_A and F_B, where the full-spectrum frequency feature vector $f = [f_1; f_2]$. Then, the input feature vector to F_A is $[f_1; 0]$ and to F_B is $[0; f_2]$. Since the input feature space (frequencies) is not shared amongst the individual models, the adversary cannot simply attack the ensemble by targeting common frequencies.

3.3 Partitioning Techniques

We propose two simple techniques for dividing the components amongst models. Note that both partitioning schemes aim to design all models in our ensemble as "equals" — if some models are less robust than others, then the adversary can target them to overturn the ensemble's decision.

Random Partitioning. For an ensemble of size n, this naive partitioning scheme divides the set of d frequency components into n equally-sized disjoint subsets, uniformly at random. Each model in the ensemble then receives one subset.

Saliency Partitioning. While signals for deepfake detection are distributed throughout the spectrum, there still exists a *adversarial saliency* ordering of these frequencies that determines their robustness for the deepfake detection task. For an ensemble of size n, our saliency partitioning technique is aimed at ensuring each model receives a fair proportion of salient frequencies. To this end, we follow Carlini & Wagner (2017) and Feng et al. (2022) to compute saliency values for all frequencies. This is achieved by adversarially perturbing deepfake x to $x + \delta^x$, where δ^x is the perturbation computed with an unbounded l_∞ PGD attack until attack success or 1000 steps, and computing saliency s_i for the ith frequency as

$$s_i = \mathbb{E}_{x \in \mathcal{X}} \nabla f(x + \delta^x)_i \cdot \delta_i^x \tag{1}$$

where subscript i denotes the ith component. Intuitively, higher gradients and larger perturbation magnitudes imply larger saliencies. Frequencies are then ordered by their saliencies, and distributed in a round-robin fashion amongst the models.

3.4 Adversarial Subspace of Disjoint Ensembles

We now show that an ensemble of disjoint frequency models increases robustness against adversarial examples by reducing the dimension of the adversarial subspace. For a single model $\mathcal{F}$ and input $\mathbf{x}$, Tramèr et al. (2017b) approximate the $k-$dimensional adversarial subspace as the span of orthogonal perturbations $\mathbf{r_1}, \cdots, \mathbf{r_k} \in \mathbb{R}^d$ such that $\mathbf{r_i}^\intercal \mathbf{g} \geq \gamma \; \forall \; 1 \leq i \leq k$ where $\mathbf{g} = \nabla_\mathbf{x} \mathcal{L}_\mathcal{F}(\mathbf{x}, y)$, $\mathcal{L}_\mathcal{F}$ is the loss function used to train $\mathcal{F}$, and γ is the increase in loss sufficient to cause a mis-classification. For perturbations satisfying the ℓ_2-norm, i.e. $||\mathbf{r_i}||_2 \leq \epsilon \; \forall \; 1 \leq i \leq k$, the adversarial dimension k is bounded by $\frac{\epsilon^2 ||\mathbf{g}||_2^2}{\gamma^2}$ (tight). In what follows, we extend this result and provide bounds for dimensionality of the shared adversarial subspace between n disjoint models. We provide tight bounds for both ℓ_2 and ℓ_∞ norms in Lemma 3.1 and Lemma 3.2 respectively (with detailed proofs in Appendix A.1). We consider these bounds for two voting mechanisms: (1) majority, where the ensemble outputs deepfake if at least $\lceil n/2 \rceil$ classifiers predict deepfake, and (2) at-least-one, where the classifier outputs deepfake if at least one classifier predicts deepfake, otherwise it outputs real.

Lemma 3.1. *Given n disjoint models, $\mathcal{F}_1, ..., \mathcal{F}_n$, having gradients $\mathbf{g_1}, \cdots, \mathbf{g_n} \in \mathbb{R}^d$ for input-label pair $(\mathbf{x}, y)$ (where $\mathbf{g_j} = \nabla_\mathbf{x} \mathcal{L}_{\mathcal{F}_j}(\mathbf{x}, y)$), the maximum number k of orthogonal vectors $\mathbf{r_1}, \mathbf{r_2}, \cdots, \mathbf{r_k} \in \mathbb{R}^d$ satisfying $||\mathbf{r_i}||_2 \leq \epsilon$ and, $\mathbf{r_i}^\intercal \mathbf{g_j} \geq \gamma_j$ for all $1 \leq j \leq n$ (at-least-one*

voting) or for at least $\lceil \frac{n}{2} \rceil$ models (majority voting), for all $1 \leq i \leq k$ is given by:

$$k = \min\left(d, \left\lfloor \frac{\epsilon^2}{\left(\sum_{j=1}^{n} \gamma_j\right)^2} \sum_{j=1}^{n} ||\mathbf{g_j}||_2^2 \right\rfloor\right) \quad \textit{(at-least-one voting)} \tag{2}$$

$$k \leq \min\left(d, \left\lfloor \max_{|K|=\lceil \frac{n}{2} \rceil} \frac{\epsilon^2}{\left(\sum_{j \in K} \gamma_j\right)^2} \sum_{j \in K} ||\mathbf{g_j}||_2^2 \right\rfloor\right) \quad \textit{(majority voting)} \tag{3}$$

$$k \geq \min\left(d, \left\lfloor \min_{|K|=\lceil \frac{n}{2} \rceil} \frac{\epsilon^2}{\left(\sum_{j \in K} \gamma_j\right)^2} \sum_{j \in K} ||\mathbf{g_j}||_2^2 \right\rfloor\right) \quad \textit{(majority voting)} \tag{4}$$

Lemma 3.2. *Given n disjoint models, $\mathcal{F}_1, ..., \mathcal{F}_n$, having gradients $\mathbf{g_1}, \cdots, \mathbf{g_n} \in \mathbb{R}^d$ for input-label pair $(\mathbf{x}, y)$ (where $\mathbf{g_j} = \nabla_{\mathbf{x}} \mathcal{L}_{\mathcal{F}_j}(\mathbf{x}, y)$), the maximum number k of orthogonal vectors $\mathbf{r_1}, \mathbf{r_2}, \cdots, \mathbf{r_k} \in \mathbb{R}^d$ satisfying $||\mathbf{r_i}||_\infty \leq \epsilon$ and $\mathbb{E}[\mathbf{g_j}^\intercal \mathbf{r_i}] \geq \gamma_j$ for all $1 \leq j \leq n$ (at-least-one voting) or for at least $\lceil \frac{n}{2} \rceil$ models (majority voting), for all $1 \leq i \leq k$*

$$k = \min\left(d, \left\lfloor \min\left(\frac{\epsilon^2 ||\mathbf{g_1}||_1^2}{n^2 \gamma_1^2}, ..., \frac{\epsilon^2 ||\mathbf{g_n}||_1^2}{n^2 \gamma_n^2}\right) \right\rfloor\right) \quad \textit{(at-least-one voting)} \tag{5}$$

$$k = \min\left(d, \left\lfloor \textit{median}\left(\frac{\epsilon^2 ||\mathbf{g_1}||_1^2}{n^2 \gamma_1^2}, ..., \frac{\epsilon^2 ||\mathbf{g_n}||_1^2}{n^2 \gamma_n^2}\right) \right\rfloor\right) \quad \textit{(majority voting)} \tag{6}$$

Takeaways. If all n disjoint models in the ensemble are "near-identical" (as expected per our saliency partitioning scheme), i.e., $||\mathbf{g_1}||_2^2 \approx \cdots \approx ||\mathbf{g_n}||_2^2$ and $\gamma_1 \approx \cdots \approx \gamma_n$, then Lemma 3.1 for at-least-one voting reduces to $k \approx \min\left(d, \left\lfloor \frac{\epsilon^2 ||\mathbf{g_1}||_2^2}{n \gamma_1^2} \right\rfloor\right)$. This implies that an ensemble of n disjoint models offers potential reduction in dimensionality of the adversarial subspace by a factor of n compared to any individual constituent disjoint model. Similar interpretation holds for Lemma 3.2, where reductions are now by a factor of n^2.

Further, we use Tramèr et al. (2017a)'s GAAS technique to estimate the dimension of the adversarial subspace in Appendix A.2. We observe that individual disjoint models exhibit lower dimension values as compared to a single model trained on the full frequency spectrum[3]. Additional analysis of individual models in Section 4.4 confirms this. This implies that ensembling such disjoint models leads to further reduction in dimensionality of the adversarial subspace.

4 Experimental Evaluation

In the following, we detail experiments to evaluate utility and robustness of D3 ensembles. We consider an adversarially trained version of a state-of-the-art full-spectrum deepfake detector (Frank et al., 2020), as well as several existing ensemble-based adversarial example defenses as our baselines. Our experiments broadly aim to answer the following questions:

Q1. What is the natural deepfake detection performance of D3 ensembles vs. a full-spectrum detector?

A1. D3 ensembles preserve the natural accuracy of a full-spectrum model — we observe reductions of less than 1% in AUC-ROC score (see Section 4.2 and Appendix A.3.1). This respectable performance can be attributed to the redundancy of relevant artifacts in the frequency space. In contrast, ensembles with partitioning in the pixel space suffer from drops of 8% in scores.

[3]Intuitively, this can be attributed to each disjoint model receiving fewer non-robust features, but continuing to perform well due to the redundancy observation.

Q2. What is the performance of D3 ensembles under white-box and black-box settings?

A2. Our ensembles offer significant robustness improvements against both white-box and black-box attacks crafted using the popular AutoAttack benchmark (Croce & Hein, 2020b) that tries multiple state-of-the-art attacks on models. For both ℓ_∞ and ℓ_2 perturbation norms, D3 continues to exhibit high adversarial accuracies (e.g., $> 99.5\%$ for $\ell_\infty, \epsilon = 32/255$) where existing defenses fail. D3 continues to offer accuracies greater than 61% ($\ell_\infty, \epsilon = 8/255$) and even 100% ($\ell_2, \epsilon = 1$) when attack steps are increased to 1000, a setting where existing state-of-the-art defenses are reduced to 0% accuracy (see Section 4.3).

Q3. How does choice of partitioning scheme and ratio impact robustness?

A3. Individual disjoint models obtained via saliency partitioning are significantly more robust than a full spectrum model. These improvements still exist for random partitioning, but are not as large. Further, individual models with partitioning ratios of 50% and 25% outperform a full spectrum trained model (see Section 4.4), with ratios beyond 25% not improving robustness.

4.1 Experimental Setup

We adopt the following settings to evaluate D3 for detecting deepfakes and adversarial deepfakes.

Datasets and Pre-processing. We primarily perform our experiments using a dataset comprising GAN-generated images of individuals. Deepfake images are generated using the state-of-the-art StyleGAN trained on the 128x128 Flickr-Faces HQ (FFHQ) dataset of celebrity headshots (Karras et al., 2019). Real images are obtained from FFHQ. We use 50,000 images for training, 10,000 for validation, and 10,000 for testing sets. Finally, we transform all deepfake images to their frequency space representation using the 2D-DCT function (Ahmed et al., 1974). We also evaluate D3 using other datasets, for which details (e.g., training splits) are provided in Appendix A.3.4. These include images from BigGAN (Brock et al., 2018) (conditional GAN trained on ImageNet (Deng et al., 2009)), StarGAN (Choi et al., 2020) (image-to-image conditional GAN trained on CelebA-HQ (Karras et al., 2018)), and other types of deepfakes, i.e., FaceSwap and NeuralTextures deepfakes from the FaceForensics++ dataset (Rössler et al., 2019).

D3 **Architecture and Training.** All models in our D3 ensembles implement the same shallow four-layer CNN employed by the baseline Frank et al. (2020) frequency-space defense. All models are adversarially trained with PGD-10 attacks (Madry et al., 2018) on deepfake images, by minimizing the binary cross-entropy loss with the Adam optimizer and an initial learning rate of 0.001. We use a batch size of 512 for a maximum of 20 epochs (with early stopping based on AUC-ROC over the validation set). All models are implemented using the PyTorch v1.6.0 framework for Python.

D3 **Configurations.** We consider two configurations of our ensemble that partition frequency components into 2 or 4 disjoint subsets, i.e., ensembles of size $n = 2$ and $n = 4$ respectively. We select these values of n based on analysis presented in Section 4.4. For the remainder of this section, we refer to these configurations as D3-R(2), D3-R(4) (for ensembles of size $n = 2$ or $n = 4$ that use the random partitioning strategy), and D3-S(2), D3-S(4) (for ensembles that use the saliency partitioning strategy). Ensemble decisions are obtained via a voting function that computes the mean logits of n models.

Baselines. We consider an adversarially trained (AT) version of Frank et al. (2020)'s full spectrum frequency-space classifier, as well as several ensemble-based defenses against adversarial examples: GAL (Kariyappa & Qureshi, 2019), ADP (Pang et al., 2019), DVERGE (Yang et al., 2020) as our baselines. TRS (Yang et al., 2021) performed poorly for deepfake detection - we weren't able to get good natural performance (likely due to the regularizer not converging over the frequency space). For all baselines, we denote the ensemble size in parentheses, e.g., ADP(4). Additional baseline details are provided in Appendix A.3.2.

4.2 Natural Deepfake Detection Performance

We evaluate deepfake detection AUC-ROC scores of Frank et al. (2020)'s full spectrum frequency-space classifier, and of all D3 configurations discussed in Section 4.1. We observe that all ensembles — even the D3-R(4) and D3-S(4) ensembles where individual models use 25% of frequency components — achieve scores over 99% (detailed numbers are deferred to Table 4 of Appendix A.3.1).

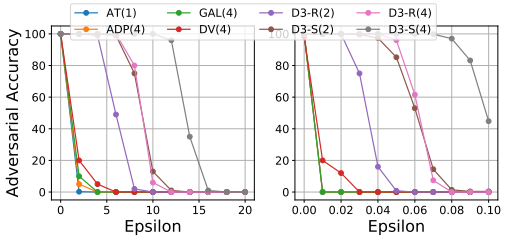

Figure 3: Adversarial accuracy of D3 and baselines as perturbation budget is increased (ℓ_2 on the left, ℓ_∞ on the right).

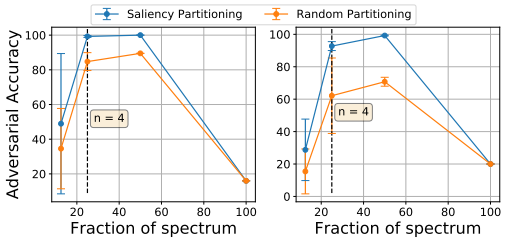

Figure 4: Expected adversarial accuracy (ℓ_2 on the left, ℓ_∞ on the right) of individual models at different partitioning ratios $\in [0, 100]$.

We emphasize the importance of frequency-space redundancy in enabling our partitioning scheme, allowing D3 to achieve these scores. To this end, we also compute scores obtained from ensembles that do not apply DCT to images, i.e., for D3 ensembles in the pixel space. Each of these ensembles exhibit considerably lower performances as artifacts are not evenly distributed throughout the pixel space. For instance, D3-S(4) obtains AUC-ROC score of only 93.83% using pixel features as compared to 99.95% in the frequency space. We again refer the reader back to Figure 2 to visualize this effect.

Table 1: Adversarial accuracies for ℓ_∞ perturbation attacks. We present accuracies for all D3 configurations, for the AT (adversarial training) baseline, and for ensemble-based baselines ADP, GAL, and DVERGE (DV). Parentheses denote the number of models used for defenses and the number steps used for attacks.

Attacks	ϵ	AT(1)	ADP(4)	GAL(4)	DV(4)	D3-R(2)	D3-S(2)	D3-R(4)	D3-S(4)
APGD-CE(50)	1/255	7.6	1.0	0.2	28.0	98.2	**100.0**	99.8	**100.0**
	4/255	0.2	0.0	0.0	21.5	97.8	**100.0**	99.2	**100.0**
	8/255	0.0	0.0	0.0	21.5	97.2	**100.0**	98.4	**100.0**
	16/255	0.0	0.0	0.0	0.0	6.0	96.2	83.8	**100.0**
APGD-CW(50)	1/255	7.4	2.6	0.4	28.0	98.4	**100.0**	99.8	**100.0**
	4/255	0.0	0.0	0.0	21.5	97.8	**100.0**	99.2	**100.0**
	8/255	0.0	0.0	0.0	21.5	97.4	**100.0**	98.6	**100.0**
	16/255	0.0	0.0	0.0	0.0	7.2	96.2	91.6	**100.0**
FAB	4/255	**100.0**	99.4	96.6	71.5	99.6	99.0	**100.0**	99.5
	16/255	**100.0**	99.4	72.8	69.0	99.6	99.0	**100.0**	99.5
	32/255	61.6	93.2	0.2	65.0	32.6	98.0	**99.5**	**99.5**
	64/255	0.0	4.8	0.0	0.0	0.0	5.8	0.0	**9.5**
Square	4/255	99.8	96.4	96.0	28.0	99.4	98.2	**99.6**	97.0
	16/255	92.0	66.6	51.0	28.0	96.8	98.2	**99.4**	96.6
	32/255	25.8	13.6	6.6	21.0	50.8	94.8	88.0	**96.2**
	64/255	0.0	0.4	0.0	0.5	0.4	45.2	4.0	**95.0**
AutoAttack (all above)	1/255	3.9	0.5	0.3	3.7	98.8	**100.0**	99.7	**100.0**
	4/255	0.0	0.0	0.0	0.0	98.8	**100.0**	99.7	**100.0**
	8/255	0.0	0.0	0.0	0.0	91.7	99.9	99.7	**100.0**
	16/255	0.0	0.0	0.0	0.0	1.2	93.8	82.6	**100.0**

4.3 Robustness Against Adversarial Examples

We evaluate robustness of D3 and baselines against attacks in both the white-box and black-box settings. We follow prior work on evaluating adversarial robustness (Yang et al., 2021) and employ *adversarial accuracy* (fraction of correctly classified adversarial examples) as our performance metric. A higher adversarial accuracy implies more robustness. All attacks are crafted using the AutoAttack benchmark, which is widely accepted as an evaluation standard for adversarial examples (Croce & Hein, 2020b). White-box attacks include the adaptive step-size PGD attacks using cross-entropy

Table 2: Adversarial accuracies for ℓ_2 perturbation attacks for same configurations as in Table 1

Attacks	ϵ	AT(1)	ADP(4)	GAL(4)	DV(4)	D3-R(2)	D3-S(2)	D3-R(4)	D3-S(4)
APGD-CE(50)	0.5	44.0	25.0	5.4	45.5	98.4	**100.0**	99.8	**100.0**
	1	16.0	1.8	1.8	24.5	97.2	**100.0**	98.9	**100.0**
	5	0.0	0.0	0.0	21.5	96.0	**100.0**	98.2	**100.0**
	10	0.0	0.0	0.0	0.0	1.2	76.2	63.6	**100.0**
APGD-CW(50)	0.5	41.4	35.8	4.4	39.5	99.4	**100.0**	99.8	**100.0**
	1	16.6	4.4	0.8	27.5	97.8	**100.0**	98.9	**100.0**
	5	0.2	0.0	0.0	21.5	97.2	**100.0**	97.0	**100.0**
	10	0.0	0.0	0.0	0.0	3.6	84.2	70.4	**100.0**
FAB	10	99.4	99.6	39.6	67.5	97.6	99.0	**100.0**	**100.0**
	20	20.4	81.0	0.0	64.5	0.8	**99.0**	54.5	98.5
	40	0.0	0.0	0.0	0.0	0.0	0.0	0.0	0.0
	80	0.0	0.0	0.0	0.0	0.0	0.0	0.0	0.0
Square	10	99.0	94.4	94.0	13.0	**100.0**	99.0	**100.0**	99.4
	20	83.8	79.8	65.6	10.0	98.2	99.0	**99.8**	99.6
	40	33.2	32.0	6.4	7.5	56.4	97.0	86.2	**99.6**
	80	1.0	0.0	0.0	0.0	0.0	22.2	2.4	**95.8**
AutoAttack (all above)	0.5	32.9	14.1	3.8	14.5	98.7	**100.0**	99.8	**100.0**
	1	7.8	0.4	0.4	1.7	98.7	**100.0**	99.8	**100.0**
	5	0.0	0.0	0.0	0.0	97.2	**100.0**	99.8	**100.0**
	10	0.0	0.0	0.0	0.0	0.3	71.4	42.5	**100.0**

Table 3: Adversarial accuracies for APGD-CE attack at $\ell_2 = 1$ and $\ell_\infty = 8/255$ under increasing steps. We present accuracies for all D3 configurations, for the AT (adversarial training) baseline, and for ensemble-based baselines ADP, GAL, and DVERGE (DV). Parentheses denote the number of models used.

Steps	AT(1)	ADP(4)	GAL(4)	DV(4)	D3-R(2)	D3-S(2)	D3-R(4)	D3-S(4)
				ℓ_2				
50	16.6	2.5	1.5	24.5	**100.0**	**100.0**	**100.0**	**100.0**
500	0.0	0.0	0.0	21.5	63.0	98.6	99.0	**100.0**
1000	0.0	0.0	0.0	0.0	34.0	85.5	94.5	**100.0**
				ℓ_∞				
50	0.0	0.0	0.0	21.5	98.0	**100.0**	**100.0**	**100.0**
500	0.0	0.0	0.0	18.5	0.0	2.0	49.0	**92.0**
1000	0.0	0.0	0.0	0.0	0.0	0.5	8.0	**61.0**

(APGD-CE) and Carlini-Wagner (APGD-CW) loss functions as well as the Fast Adaptive Boundary (FAB) attack. Black-box attacks include Square attack (Andriushchenko et al., 2020).

Table 1 presents adversarial accuracies under a variety of ℓ_∞ perturbation budgets. We observe that D3 (specifically, the D3-S(4) configuration) outperforms all baselines under white-box settings, with adversarial accuracies no less than 99.5% for attack budgets as large as $\epsilon = 32/255$. In contrast, the closest performing baseline (DVERGE) demonstrates accuracies as low as 21.5% under the same settings. This performance gap tends to widen under large perturbation budgets. Similar trends also hold under black-box attacks, where D3 continues to outperform all baselines even on perturbation budgets of $\epsilon = 64/255$. Finally, Table 2 presents adversarial accuracies under a variety of ℓ_2 perturbation budgets, where we observe trends identical to those in ℓ_∞ attacks.

Table 3 present results for ℓ_2 and ℓ_∞ attacks where we increase the number of iteration steps in the white-box APGD-CE attack. While D3's accuracy does drop to 61% under 1000 attack steps, it continues to outperform all baselines (which unanimously drop to 0%). Figure 3 demonstrates that above trends continue to hold under increased perturbation budgets.

We also evaluate D3 on other GAN datasets, where similar findings hold — see Appendix A.3.4 for details. Appendix A.3.3 also includes results for "baseline" attack strategies, such as transfer attacks from a full-spectrum model, which expectedly do not succeed.

4.4 Impact of Partitioning Scheme on Robustness

In Section 4.3, we observed that ensembles constructed using our saliency partitioning strategy (D3-S(2) and D3-S(4)) demonstrated higher adversarial accuracies than those using our random partitioning strategy (D3-R(2) and D3-R(4)) under all attacks. Both strategies outperformed the full-spectrum detector. We explain these results by examining the robustness of the individual constituent models under both strategies.

Figure 4 plots the expected adversarial accuracy over the individual models in the ensemble for both schemes (using the same APGD-50 attack on 1000 images for ℓ_2 $\epsilon = 1$, ℓ_∞ $\epsilon = 4/255$). We observe that all the individual models (looking at 50% and 25%) are more robust than the full-spectrum (100%) detector, thus satisfying the conditions in Lemmas 3.1 and 3.2. For individual models looking at 12.5%, this is not the case (see high standard deviations). Additionally, individual models produced using saliency partitioning are more robust than those using random (due to proportionate distribution of robust/non-robust frequencies), suggesting further reduction in adversarial subspace dimensionality when ensembling. Finally, we note that arbitrarily partitioning beyond 25% does not improve robustness of individual models, suggesting diminishing gains beyond an ensemble of $n = 4$ models.

5 Discussion

Below we address discussion points that may arise around D3.

Societal impact and limitations. The realism of modern deepfakes raises several societal and security threats; D3 is a step towards mitigating that. Nonetheless, adversarial deepfakes also have benign use cases, e.g., anonymization of an end-user on an online network; D3 could prevent such anonymization. We believe that the benefits of D3 outweigh such potential concerns.

Concerns of gradient obfuscation. Athalye et al. (2018) showed that many defenses lead to obfuscating gradients, which is known to be a broken defense. We emphasize that D3 does not fall under this category of defenses — D3 only uses DCT as an input transformation which is a well studied, differentiable matrix multiplication used in signal processing. Then, each classifier simply looks at a disjoint subset of these frequencies. Nonetheless, we follow Athalye et al. (2018)'s five recommended guidelines for identifying obfuscated gradients, and find that (a) one-step attacks do *not* perform better than iterative attacks, (b) black-box attacks do *not* perform better than white-box attacks, (c) unbounded attacks *do* reach 100% success, (d) random sampling does *not* find more adversarial examples, and (e) increasing distortion *does* increase attack success. These findings point to obfuscated gradients not being a concern.

Applicability to domains other than deepfake detection. We presented D3 as a ensemble framework for adversarially robust deepfake detection. However, we hypothesize that this approach could be applied to any classification task that exhibits redundancy in a feature space. While we are unaware of such a space for the popular CIFAR10 and ImageNet classification tasks, there are several classification tasks in, say, the audio domain that exhibit redundancy in features, e.g., keyword spotting and fake speech detection. Exploring this hypothesis is an interesting future research direction.

6 Conclusions

In this paper, we present D3, an ensemble-based approach to deepfake detection that significantly improves adversarial robustness beyond adversarial training and prior ensemble-based adversarial example defenses. We observe redundancy in the frequency-space artifacts of GAN-generated deepfakes, and use this redundancy to build disjoint ensembles that prevent the adversary from simply targeting shared features. We formally show that our ensemble approach reduces the dimensionality of the subspace in which adversarial deepfakes lie, and empirically validate that D3 offers significant gains in adversarial robustness under multiple attacks.

REFERENCES

Nasir Ahmed, T_ Natarajan, and Kamisetty R Rao. Discrete Cosine Transform. *IEEE Transactions on Computers*, 1974.

Maksym Andriushchenko, Francesco Croce, Nicolas Flammarion, and Matthias Hein. Square Attack: a query-efficient black-box adversarial attack via random search . In *Proceedings of European Conference on Computer Vision*, 2020.

Anish Athalye, Nicholas Carlini, and David Wagner. Obfuscated Gradients Give a False Sense of Security: Circumventing Defenses to Adversarial Examples. In *Proceedings of International Conference on Machine Learning*, 2018.

Pierre Baldi. Autoencoders, Unsupervised Learning, and Deep Architectures. In *Proceedings of ICML Workshop on Unsupervised and Transfer Learning*, 2012.

Battista Biggio, Igino Corona, Davide Maiorca, Blaine Nelson, Nedim Šrndić, Pavel Laskov, Giorgio Giacinto, and Fabio Roli. Evasion Attacks Against Machine Learning at Test Time. In *Joint European Conference on Machine Learning and Knowledge Discovery in Databases*, 2013.

Andrew Brock, Jeff Donahue, and Karen Simonyan. Large scale gan training for high fidelity natural image synthesis. *arXiv preprint arXiv:1809.11096*, 2018.

Nicholas Carlini and Hany Farid. Evading deepfake-image detectors with white-and black-box attacks. In *Proceedings of the IEEE/CVF Conference on Computer Vision and Pattern Recognition Workshops*, pp. 658–659, 2020.

Nicholas Carlini and David Wagner. Towards evaluating the robustness of neural networks. In *2017 IEEE Symposium on Security and Privacy (SP)*, pp. 39–57. IEEE, 2017.

Yunjey Choi, Youngjung Uh, Jaejun Yoo, and Jung-Woo Ha. Stargan v2: Diverse image synthesis for multiple domains. In *Proceedings of the IEEE Conference on Computer Vision and Pattern Recognition*, 2020.

Samantha Cole. Ai-assisted fake porn is here and we're all f****d. `https://www.vice.com/en_us/article/gydydm/gal-gadot-fake-ai-porn`, 2017.

Francesco Croce and Matthias Hein. Minimally distorted adversarial examples with a fast adaptive boundary attack. In *International Conference on Machine Learning*, pp. 2196–2205. PMLR, 2020a.

Francesco Croce and Matthias Hein. Reliable evaluation of adversarial robustness with an ensemble of diverse parameter-free attacks. In *International conference on machine learning*, pp. 2206–2216. PMLR, 2020b.

Jia Deng, Wei Dong, Richard Socher, Li-Jia Li, Kai Li, and Li Fei-Fei. Imagenet: A large-scale hierarchical image database. In *2009 IEEE conference on computer vision and pattern recognition*, pp. 248–255. Ieee, 2009.

Ricard Durall, Margret Keuper, Franz-Josef Pfreundt, and Janis Keuper. Unmasking deepfakes with simple features. *arXiv preprint arXiv:1911.00686*, 2019.

Ryan Feng, Neal Mangaokar, Jiefeng Chen, Earlence Fernandes, Somesh Jha, and Atul Prakash. Graphite: Generating automatic physical examples for machine-learning attacks on computer vision systems. *arXiv preprint arXiv:2002.07088*, 2022.

Joel Frank, Thorsten Eisenhofer, Lea Schönherr, Asja Fischer, Dorothea Kolossa, and Thorsten Holz. Leveraging frequency analysis for deep fake image recognition. In *International Conference on Machine Learning*, pp. 3247–3258. PMLR, 2020.

Ian Goodfellow, Jean Pouget-Abadie, Mehdi Mirza, Bing Xu, David Warde-Farley, Sherjil Ozair, Aaron Courville, and Yoshua Bengio. Generative adversarial nets. *Advances in neural information processing systems*, 27, 2014.

Ian Goodfellow, Jonathon Shlens, and Christian Szegedy. Explaining and harnessing adversarial examples. In *International Conference on Learning Representations*, 2015. URL http://arxiv.org/abs/1412.6572.

Warren He, James Wei, Xinyun Chen, Nicholas Carlini, and Dawn Song. Adversarial example defense: Ensembles of weak defenses are not strong. In *11th {USENIX} workshop on offensive technologies ({WOOT} 17)*, 2017.

Andrew Ilyas, Shibani Santurkar, Dimitris Tsipras, Logan Engstrom, Brandon Tran, and Aleksander Madry. Adversarial examples are not bugs, they are features. *Advances in neural information processing systems*, 32, 2019.

Sanjay Kariyappa and Moinuddin K Qureshi. Improving adversarial robustness of ensembles with diversity training. *arXiv preprint arXiv:1901.09981*, 2019.

Tero Karras, Timo Aila, Samuli Laine, and Jaakko Lehtinen. Progressive growing of gans for improved quality, stability, and variation. In *International Conference on Learning Representations*, 2018.

Tero Karras, Samuli Laine, and Timo Aila. A style-based generator architecture for generative adversarial networks. In *Proceedings of the IEEE/CVF Conference on Computer Vision and Pattern Recognition*, pp. 4401–4410, 2019.

Davis E King. Dlib-ml: A Machine Learning Toolkit. *JMLR*, 2009.

Alex Krizhevsky, Geoffrey Hinton, et al. Learning multiple layers of features from tiny images. 2009.

Aleksander Madry, Aleksandar Makelov, Ludwig Schmidt, Dimitris Tsipras, and Adrian Vladu. Towards deep learning models resistant to adversarial attacks. In *International Conference on Learning Representations*, 2018. URL https://openreview.net/forum?id=rJzIBfZAb.

Paris Martineau. Facebook removes accounts with ai-generated profile photos. https://www.wired.com/story/facebook-removes-accounts-ai-generated-photos/, 2019.

Scott McCloskey and Michael Albright. Detecting gan-generated imagery using color cues. *arXiv preprint arXiv:1812.08247*, 2018.

Lakshmanan Nataraj, Tajuddin Manhar Mohammed, BS Manjunath, Shivkumar Chandrasekaran, Arjuna Flenner, Jawadul H Bappy, and Amit K Roy-Chowdhury. Detecting gan generated fake images using co-occurrence matrices. *Electronic Imaging*, 2019(5):532–1, 2019.

Paarth Neekhara, Brian Dolhansky, Joanna Bitton, and Cristian Canton Ferrer. Adversarial threats to deepfake detection: A practical perspective. In *Proceedings of the IEEE/CVF Conference on Computer Vision and Pattern Recognition*, pp. 923–932, 2021.

Tianyu Pang, Kun Xu, Chao Du, Ning Chen, and Jun Zhu. Improving adversarial robustness via promoting ensemble diversity. In *International Conference on Machine Learning*, pp. 4970–4979. PMLR, 2019.

Andreas Rössler, Davide Cozzolino, Luisa Verdoliva, Christian Riess, Justus Thies, and Matthias Nießner. FaceForensics++: Learning to detect manipulated facial images. In *International Conference on Computer Vision (ICCV)*, 2019.

Christian Szegedy, Wojciech Zaremba, Ilya Sutskever, Joan Bruna, Dumitru Erhan, Ian Goodfellow, and Rob Fergus. Intriguing properties of neural networks. In *International Conference on Learning Representations*, 2014. URL http://arxiv.org/abs/1312.6199.

Florian Tramèr, Alexey Kurakin, Nicolas Papernot, Ian Goodfellow, Dan Boneh, and Patrick McDaniel. Ensemble adversarial training: Attacks and defenses. *arXiv preprint arXiv:1705.07204*, 2017a.

Florian Tramèr, Nicolas Papernot, Ian Goodfellow, Dan Boneh, and Patrick McDaniel. The space of transferable adversarial examples. *arXiv preprint arXiv:1704.03453*, 2017b.

Sheng-Yu Wang, Oliver Wang, Richard Zhang, Andrew Owens, and Alexei A Efros. Cnn-generated images are surprisingly easy to spot... for now. In *Proceedings of the IEEE/CVF Conference on Computer Vision and Pattern Recognition*, pp. 8695–8704, 2020.

Huanrui Yang, Jingyang Zhang, Hongliang Dong, Nathan Inkawhich, Andrew Gardner, Andrew Touchet, Wesley Wilkes, Heath Berry, and Hai Li. Dverge: diversifying vulnerabilities for enhanced robust generation of ensembles. *Advances in Neural Information Processing Systems*, 33: 5505–5515, 2020.

Zhuolin Yang, Linyi Li, Xiaojun Xu, Shiliang Zuo, Qian Chen, Pan Zhou, Benjamin Rubinstein, Ce Zhang, and Bo Li. Trs: Transferability reduced ensemble via promoting gradient diversity and model smoothness. *Advances in Neural Information Processing Systems*, 34, 2021.

Ning Yu, Larry S Davis, and Mario Fritz. Attributing fake images to gans: Learning and analyzing gan fingerprints. In *Proceedings of the IEEE/CVF International Conference on Computer Vision*, pp. 7556–7566, 2019.

Xu Zhang, Svebor Karaman, and Shih-Fu Chang. Detecting and simulating artifacts in gan fake images. In *2019 IEEE International Workshop on Information Forensics and Security (WIFS)*, pp. 1–6. IEEE, 2019.

A Appendix

In Appendix A.1, we provide proofs for our bounds on dimensionality of the adversarial subspace of disjoint ensembles, such as D3. Appendix A.2 empirically estimates the dimension of the adversarial subspace using a combinatorial construction of orthogonal perturbations. In Appendix A.3, we provide details of our baseline configurations and attack settings for reproducibility purposes, as well as additional experimental results on other datasets. Finally, in Appendix A.4, we provide additional insight and motivation for our saliency frequency partitioning scheme.

A.1 Proofs

A.1.1 Orthogonal Gradients

Prior to providing proofs for the adversarial dimensions, we demonstrate that gradients for disjoint classifiers are always orthogonal to each other. We will use this for our later results. Given input space $\mathcal{X}$ and class-label space $\mathcal{Y}$, we have n disjoint classifiers $\mathcal{F}_1, ..., \mathcal{F}_n$. If T is the DCT transformation matrix, we can define T_i to be the transformation matrix for the classifier $\mathcal{F}_i$. Each disjoint transformation T_i has a lot of zeros. Only the rows corresponding to the unmasked frequencies of classifier $\mathcal{F}_i$ have non-zero entries. Moreover, since no frequency is shared by any two classifiers, the jth row will have non-zero entries in exactly one of the n disjoint transformation matrices, i.e. $T_i T_j^\intercal = O \; \forall i \neq j$.

Next, the n disjoint classifiers $\mathcal{F}_1, ..., \mathcal{F}_n$, where $\mathcal{F}_i : T_i \mathbf{x} \to y$, are trained using loss functions $\mathcal{L}_{\mathcal{F}_1}, ..., \mathcal{L}_{\mathcal{F}_n}$ respectively. Now, the dot product between the gradients of classifiers $\mathcal{F}_i$ and $\mathcal{F}_j$ is given by

$$\begin{aligned}
(\nabla_{\mathbf{x}} \mathcal{L}_{\mathcal{F}_i})^\intercal \left(\nabla_{\mathbf{x}} \mathcal{L}_{\mathcal{F}_j}\right) &= (T_i^\intercal \nabla_{T_i \mathbf{x}} \mathcal{L}_{\mathcal{F}_i})^\intercal \left(T_j^\intercal \nabla_{T_j \mathbf{x}} \mathcal{L}_{\mathcal{F}_j}\right) \\
&= (\nabla_{T_i \mathbf{x}} \mathcal{L}_{\mathcal{F}_i})^\intercal \, T_i T_j^\intercal \left(\nabla_{T_j \mathbf{x}} \mathcal{L}_{\mathcal{F}_j}\right) \\
&= 0
\end{aligned} \tag{7}$$

A.1.2 Proof of Lemma 3.1

From Tramèr et al. (2017b), we know that for a classifier $\mathcal{F} : \mathcal{X} \to \mathcal{Y}$ where $\mathcal{X} \in \mathbb{R}^d$ is the input space and $\mathcal{Y}^c \in \mathbb{Z}$ is the finite class label space, the dimension of the adversarial subspace

around input-label pair $(\mathbf{x}, y)$ where $\mathbf{x} \in \mathcal{X}$ and $y \in \mathcal{Y}$, is approximated by the maximal number of orthogonal perturbations $\mathbf{r_1}, \mathbf{r_2}, ..., \mathbf{r_k}$ such that $||\mathbf{r_i}||_2 \leq \epsilon$ and $\mathbf{g}^\intercal \mathbf{r_i} \geq \gamma \ \forall \ 1 \leq i \leq k$. Here, $\mathbf{g} = \nabla_{\mathbf{x}} L(\mathcal{F}(\mathbf{x}), y)$ and γ is the increase in loss function L sufficient to cause a mis-classification. Tramèr et al. (2017b) provide a tight bound for k:

$$k = \min\left(d, \left\lfloor \frac{\epsilon^2 ||\mathbf{g}||_2^2}{\gamma^2} \right\rfloor\right) \tag{8}$$

We now extend this result for n disjoint classifiers. Let $\mathbf{g}' = \frac{\sum_{j=1}^{n} \mathbf{g_j}}{n}$.
Now, for *at-least-one voting*,

$$\mathbf{g}'^\intercal \mathbf{r_i} = \frac{\sum_{j=1}^{n} \mathbf{g_j}^\intercal \mathbf{r_i}}{n} \geq \frac{\sum_{j=1}^{n} \gamma_j}{n} \quad \forall \ 1 \leq i \leq k \tag{9}$$

Applying the result from Tramèr et al. (2017b) (Equation 8) on the above inequality (Equation 9), we get:

$$\begin{aligned} k &= \min\left(d, \left\lfloor \frac{\epsilon^2 n^2 ||\mathbf{g}'||_2^2}{\left(\sum_{j=1}^{n} \gamma_j\right)^2} \right\rfloor\right) \\ &= \min\left(d, \left\lfloor \frac{\epsilon^2 \sum_{j=1}^{n} ||\mathbf{g_j}||_2^2}{\left(\sum_{j=1}^{n} \gamma_j\right)^2} \right\rfloor\right). \quad \text{(since } \mathbf{g_i}^\intercal \mathbf{g_j} = 0 \ \ \forall i \neq j \text{, using Equation 7)} \end{aligned} \tag{10}$$

Now, for *majority voting*, we again apply the results from Tramèr et al. (2017b) (Equation 8). However, the derivation now depends on the selection of $\lceil \frac{n}{2} \rceil$ models that the adversary chooses to target. To obtain the lower and upper bounds, we can select $\lceil \frac{n}{2} \rceil$ with the most and least adversarial dimensions respectively. Following a similar derivation as before, we get :

$$k \geq \min\left(d, \left\lfloor \min_{|K| = \lceil \frac{n}{2} \rceil} \frac{\epsilon^2 \sum_{j=1}^{n} ||\mathbf{g_j}||_2^2}{\left(\sum_{j=1}^{n} \gamma_j\right)^2} \right\rfloor\right) \tag{11}$$

$$k \leq \min\left(d, \left\lfloor \max_{|K| = \lceil \frac{n}{2} \rceil} \frac{\epsilon^2 \sum_{j=1}^{n} ||\mathbf{g_j}||_2^2}{\left(\sum_{j=1}^{n} \gamma_j\right)^2} \right\rfloor\right) \tag{12}$$

A.1.3 Proof of Lemma 3.2

Follow up work from Tramèr et al. (2017a) also provides a tight bound for the adversarial dimension in the ℓ_∞ case. They provide a tight bound for the number of k orthogonal perturbations $\mathbf{r_1}, ..., \mathbf{r_k} \in$

$\mathbb{R}^d$ such that $||\mathbf{r_i}||_\infty \leq \epsilon$, given by $sign(\mathbf{g})^\intercal \mathbf{r_i} = \frac{\epsilon d}{\sqrt{k}}$ $\forall 1 \leq i \leq k$ where $sign(\mathbf{g})$ is the signed gradient.

We now extend this result for n disjoint classifiers. For $\mathbf{g}' = \frac{\sum_{j=1}^{n} \mathbf{g_j}}{n}$, since $\mathbf{g_j}'s$ are non-zero only on non-overlapping dimensions, we can see that $sign(\mathbf{g}')^\intercal r = \sum_{j=1}^{n} sign(\mathbf{g_j})^\intercal r$ $\forall \mathbf{r} \in \mathbb{R}^d$. Applying the above results here, we get

$$\sum_{j=1}^{n} sign(\mathbf{g_j})^\intercal \mathbf{r_i} = \frac{\epsilon d}{\sqrt{k}} \; \forall 1 \leq i \leq k \tag{13}$$

Now, similar to Tramèr et al. (2017a), we compute the perturbation magnitude along a random permutation of the signed gradient. For each $1 \leq j \leq n$ and $1 \leq i \leq k$, we get :

$$\begin{aligned} \mathbb{E}[\mathbf{g_j}^\intercal \mathbf{r_i}] &= \mathbb{E}\left[\sum_{p=1}^{d} |g_j^{(p)}| \cdot sign(g_j^{(p)}) \cdot r_i^{(p)}\right] \\ &= \sum_{p=1}^{d} |g_j^{(p)}| \mathbb{E}\left[sign(g_j^{(p)}) \cdot r_i^{(p)}\right] \\ &= \frac{\epsilon ||\mathbf{g_j}||_1}{n\sqrt{k}} \end{aligned} \tag{14}$$

A.2 Estimating Dimension of Adversarial Subspace

In this section, we use Tramèr et al. (2017a)'s combinatorial construction to find k orthogonal adversarial directions for a full spectrum (100%) model as well as individual models that use a fraction of the frequency features. The frequency features are selected using the saliency partitioning scheme (Section 3.3).

We construct orthogonal perturbations by multiplying the row vectors from a Regular Hadamard matrix component-wise with $sign(\mathbf{g})$ where $\mathbf{g}$ is the model gradient. We consider 3 settings, based on fraction of frequency features - 100%, 50% and 25%. For each setting, we then select 1000 correctly classified inputs, and compute loss gradients for each input. Using a regular Hadamard Matrix of order w, the above construction gives w orthogonal directions. Out of these w, the number of directions that are actually adversarial provide an estimate for k. We run the analysis for $w \in \{4, 16, 36, 64, 100\}$, and select the maximum value.

Figure 5 plots the proportion of images (out of 1000) with at least k adversarial dimensions. We observe that both the 50% and 25% settings have fewer images with high dimension of the adversarial subspace. These results support the analysis done in Section 3.4. Further, the reduced adversarial dimension for the 50% and 25% settings is consistent with their improved robustness over the full spectrum (100%) model (Section 4.4).

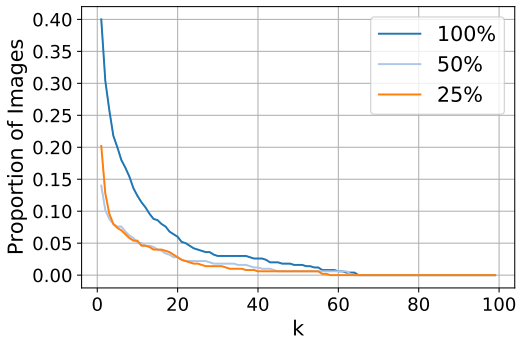

Figure 5: Distribution of adversarial saliency magnitudes for frequency components.

A.3 Additional Evaluation Details

A.3.1 Natural Deepfake Detection Performance

Type	AT(1)	D3-R(2)	D3-S(2)	D3-R(4)	D3-S(4)
Frequency	99.99	99.96	99.98	99.93	99.95
Pixel	97.59	90.42	96.45	90.11	93.83

Table 4: Natural deepfake detection AUC-ROC scores of D3 ensembles, in comparison with a full-spectrum detector, i.e., AT(1).

A.3.2 Details for Baselines

In this section, we provide additional details for all models/ensembles used for the baseline evaluation. We implement all the baselines using the four-layer CNN employed by Frank et al. (2020).

Adversarial-Training (Madry et al., 2018). We employ adversarial training, which involves training the CNN on adversarial examples for deepfake images only (not real images). Adversarial examples are constructed using the PGD-10 attack (i.e., 10 steps of gradient descent), with $\epsilon = 1/255$ and a step size of 0.001. We train for 20 epochs with a batch size of 512.

GAL (Kariyappa & Qureshi, 2019). This approach minimizes transferability via a regularizer. Specifically, GAL minimizes the cosine similarity between individual models' loss gradients. We set the coefficient for standard cross-entropy loss as 1, and for the cosine loss as 0.5. We train for 35 epochs with a batch size of 128.

ADP (Pang et al., 2019). This approach also minimizes transferability via a regularizer. The primary term in ADP's regularizer maximizes the volume spanned by individual model's non-prediction output vectors, i.e., the vectors obtained by removing the top-confidence class, so as to maximize diversity without affecting accuracy. We set coefficients for standard cross-entropy loss as 1, for the volume term in the regularizer as 0.5, and for the entropy term in the regularizer as 2. We train for 1 epoch with a batch size of 128.

DVERGE (Yang et al., 2020). DVERGE minimizes transferability by adversarially training individual models on "adversarial features" constructed against other models in the ensemble. Adversarial features are constructed by minimizing a novel feature-distillation objective over 10 steps, with $\epsilon = 0.07$ and step size as 0.007. We train for 5 epochs with a batch size of 128.

A.3.3 Details for Attacks

We consider the following attacks for our evaluation. These attacks constitute the entire ensemble of attacks used in the AutoAttack Benchmark. We tune the attacks where necessary to get the strongest attack setting.

APGD-CE/CW (Croce & Hein, 2020b) is a step-size free variant of the standard PGD attack. It adjusts the step size during the attack based on the convergence of the loss and the overall perturbation budget. We optimize the adaptive PGD-attack on the Cross Entropy (CE) and Carlini Wagner (CW) loss functions. We use the same set of parameters for the attack as mentioned in AutoAttack Benchmark other than the step size decay parameter α which we set to 0.1 instead of 2.

FAB (Croce & Hein, 2020a) is a iterative first order attack that utilizes geometry of the decision boundary to minimize the perturbation required to cause mis-classification. We use the same set of parameters as AutoAttack.

Square (Andriushchenko et al., 2020) is an efficient black-box attack that uses random square shaped updates to approximate the decision boundary. We use the same set of parameters as AutoAttack.

We also include in Table 5 results for a "baseline" attack, in which we evaluate D3 on adversarial examples computed against a full-spectrum classifier. As expected, such adversarial examples do not evade D3.

	ℓ_2					ℓ_∞				
ϵ	0.5	1	5	10	20	1/255	4/255	8/255	16/255	32/255
Accuracy	100.0	100.0	100.0	100.0	1.4	100.0	100.0	100.0	100.0	49.1

Table 5: Adversarial accuracy of D3-S(4) under adversarial examples crafted against a full-spectrum detector.

A.3.4 Evaluation on Other Datasets

BigGAN. The BigGAN dataset comprises images GAN-generated images belonging to the 1000 classes in the ImageNet (Deng et al., 2009) dataset. Images are generated using BigGAN (Brock et al., 2018) trained on the 256x256 ImageNet dataset of 1000 object and animal classes. Images are resized to 128x128. We use 35,000 images for training, 7,500 images for validation, and 7,500 for testing sets. Corresponding real images are obtained from the ImageNet dataset.

Table 6: BigGAN adversarial accuracies for ℓ_∞ and ℓ_2 perturbation attacks for same configurations as in Table 2

Attacks	ϵ	AT(1)	ADP(4)	GAL(4)	DV(4)	D3-S(4)
			ℓ_∞			
APGD-CE(50)	1/255	16.2	9.1	41.5	5.5	**91.0**
	4/255	14.4	9.1	9.4	0.0	**90.0**
	8/255	14.4	9.1	9.4	0.0	**78.3**
	16/255	14.4	9.1	9.4	0.0	**26.6**
APGD-CW(50)	1/255	15.9	9.1	2.3	5.4	**91.0**
	4/255	14.4	9.1	43.8	0.0	**90.5**
	8/255	14.4	9.1	9.4	0.0	**79.6**
	16/255	14.4	9.1	9.4	0.0	**26.7**
			ℓ_2			
APGD-CE(50)	0.1	23.6	9.2	59.4	13.6	**91.0**
	1	16.6	9.1	27.1	2.8	**91.0**
	5	14.4	9.1	9.4	0.0	**70.5**
	10	14.4	9.1	9.4	0.0	**26.2**
APGD-CW(50)	0.1	25.1	9.3	61.6	14.5	**91.0**
	1	15.4	9.1	27.4	3.1	**91.0**
	5	14.4	9.1	9.4	0.0	**71.0**
	10	14.4	9.1	9.4	0.0	**26.2**

Table 7: StarGAN adversarial accuracies for ℓ_∞ and ℓ_2 perturbation attacks for same configurations as in Table 2

Attacks	ϵ	AT(1)	ADP(4)	GAL(4)	DV(4)	D3-S(4)
			ℓ_∞			
APGD-CE(50)	1/255	14.6	8.6	1.6	18.5	**100.0**
	4/255	0.0	0.0	0.0	3.0	**99.6**
	8/255	0.0	0.0	0.0	0.0	**0.1**
	16/255	0.0	0.0	0.0	0.0	**0.1**
APGD-CW(50)	1/255	11.5	17.4	2.3	19.3	**100.0**
	4/255	0.0	0.0	0.0	2.7	**99.8**
	8/255	0.0	0.0	0.0	0.0	**0.1**
	16/255	0.0	0.0	0.0	0.0	**0.1**
			ℓ_2			
APGD-CE(50)	0.1	45.3	87.5	13.5	25.3	**100.0**
	1	9.5	0.0	0.9	11.6	**100.0**
	5	0.0	0.0	0.0	**2.7**	0.1
	10	0.0	0.0	0.0	**2.7**	0.1
APGD-CW(50)	0.1	20.9	90.8	16.2	19.3	**100.0**
	1	3.3	0.1	0.3	5.8	**100.0**
	5	0.0	0.0	0.0	**2.7**	0.1
	10	0.0	0.0	0.0	**2.7**	0.1

StarGAN. The StarGAN dataset comprises images GAN-generated images belonging to the 1000 classes in the ImageNet (Deng et al., 2009) dataset. Images are generated using StarGAN (Choi et al., 2020) trained on the 256x256 CelebA-HQ dataset (resized from 1024x1024) of celebrity headshots (Karras et al., 2018). Since StarGAN is an image-to-Image translation GAN that changes the "style", i.e., hairstyle, eye color, etc of an existing real image, we generate images using randomly sampled styles. Images are resized to 128x128. We use 21,000 images for training, 4,500 images for validation, and 4,500 for testing sets. Corresponding real images are obtained from CelebA-HQ.

FaceForensics++ (DeepFakes and NeuralTextures.) This dataset comprises the DeepFakes and NeuralTextures subsets of the FaceForensics++ dataset (Rössler et al., 2019). These are face-swap deepfake videos generated using neural, non-GAN techniques, and are thus not the primary focus of this work. Nonetheless, we include preliminary evaluation of natural performance on these videos. We extract faces from each video frame using the dlib library (King, 2009). Face images are resized to 128x128. We use 6,265 images for training, 1,342 for validation, and 1,343 for testing.

Dataset	AT(1)	D3-S(4)
DeepFakes	98.8	90.6
NeuralTextures	94.6	80.8

Table 8: Natural accuracies of D3 and a full-spectrum classifier on non-GAN generated deepfakes from the FaceForensics++ dataset.

A.4 Understanding Frequency Partitioning

Recall that each model in our ensembles uses a subset of frequencies. However, as per Ilyas et al. (2019)'s robust features model, these frequencies can likely be categorized as either robust, or non-robust. We would like each model to receive an equal number of robust frequencies. In Section 3.3, we discussed two schemes for disjoint partitioning of frequency components — a more "naive" random partitioning, and our proposed saliency partitioning. To better visualize how saliency partitioning achieves our goal of equal distribution, Figure 6 plots a histogram of adversarial saliency magnitudes. Recall that these saliencies are computed using the gradient (and perturbation) magnitude *at the adversarial example*, i.e., our adversarial saliencies are a heuristic measure of "robustness" of each frequency component, with higher saliencies implying less robustness.

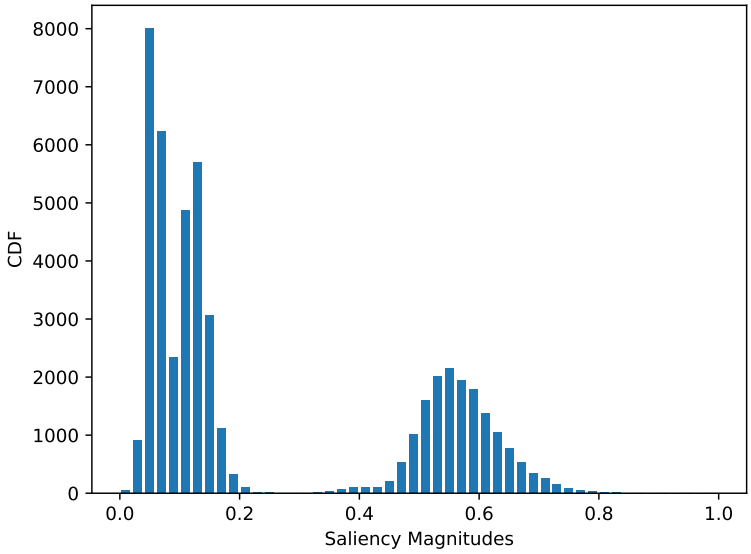

Figure 6: Distribution of adversarial saliency magnitudes for frequency components.

It is clear that there exists a large number of low-saliency (or high-robustness) frequency components with magnitudes < 0.2. If a majority of these components were allocated to a single model, only components with saliency magnitudes > 0.4 would remain for the other models. Our saliency partitioning scheme thus aims to ensure that each model in the ensemble receives a fair proportion of high-robustness components with magnitudes < 0.2.

The above analysis also leads us to ask — which frequency components are of high-saliency (low-robustness), and why? To this end, we visualize saliency magnitudes across all channels in Figure 7.

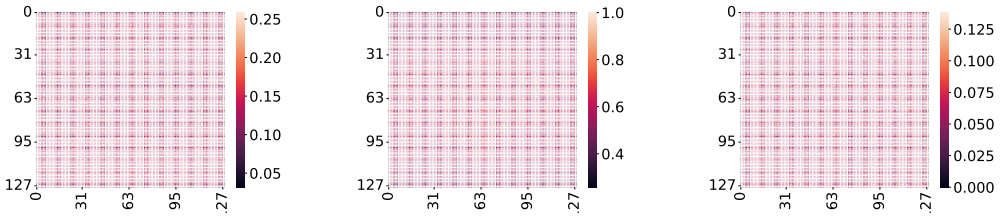

(a) R-channel (b) G-channel (c) B-channel

Figure 7: Per-channel heatmaps of adversarial saliency magnitudes. Note the grid-like pattern, matching the pattern of artifacts used for deepfake detection itself.

We observe that low-saliency (high-robustness) components are largely those are constitute the grid-like artifact pattern crucial to deepfake detection itself (see Section 3.1). All remaining components appear to be high-saliency (low-robustness). Additionally, the G-channel appears to comprise the most low-robustness components.